A&A 650, A166 (2021)
https://doi.org/10.1051/0004-6361/202040030

Astronomy & Astrophysics

Day-night differences in Mars methane suggest nighttime containment at Gale crater*

Christopher R. Webster[1], Paul R. Mahaffy[2], Jorge Pla-Garcia[3,4], Scot C. R. Rafkin[5], John E. Moores[6], Sushil K. Atreya[7], Gregory J. Flesch[1], Charles A. Malespin[2], Samuel M. Teinturier[2,8], Hemani Kalucha[6], Christina L. Smith[6], Daniel Viúdez-Moreiras[3], and Ashwin R. Vasavada[1]

[1] NASA Jet Propulsion Laboratory, California Institute of Technology, Pasadena, CA, USA
e-mail: chris.r.webster@jpl.nasa.gov
[2] NASA Goddard Space Flight Center, Greenbelt, MD, USA
[3] Centro de Astrobiología (CSIC-INTA), Madrid, Spain
[4] Space Science Institute, Boulder, CO, USA
[5] Department of Space Studies, Southwest Research Institute, Boulder, CO, USA
[6] York University, Toronto, ON, Canada
[7] University of Michigan, Ann Arbor, MI, USA
[8] GESTAR, USRA, Columbia, MD, USA

Received 1 December 2020 / Accepted 29 April 2021

ABSTRACT

We report new measurements of atmospheric methane by the Curiosity rover's Tunable Laser Spectrometer that is part of the Sample Analysis at Mars suite (TLS-SAM), finding nondetections during two daytime measurements of average value 0.05 ± 0.22 ppbv (95% confidence interval CI). These are in marked contrast with nighttime background levels of 0.52 ± 0.10 (95% CI) from four measurements taken during the same season of northern summer. This large day-night difference suggests that methane accumulates while contained near the surface at night, but drops below TLS-SAM detection limits during the day, consistent with the daytime nondetection by instruments on board the ExoMars Trace Gas Orbiter. With no evidence for methane production by the rover itself, we propose that the source is one of planetary micro-seepage. Dynamical modeling indicates that such methane release is contained within the collapsed planetary boundary layer (PBL) at night due to a combination of nocturnal inversion and convergent downslope flow winds that confine the methane inside the crater close to the point where it is released. The methane abundance is then diluted during the day through increased vertical mixing associated with a higher altitude PBL and divergent upslope flow that advects methane out of the crater region. We also report detection of a large spike of methane in June 2019 with a mean in situ value over a two-hour ingest of 20.5 ± 4 ppbv (95% CI). If near-surface production is occurring widely across Mars, it must be accompanied by a fast methane destruction or sequestration mechanism, or both.

Key words. techniques: spectroscopic – planets and satellites: atmospheres – planets and satellites: composition

1. Introduction

The quantity, distribution, and behavior of methane in the atmosphere of Mars are of great interest to the planetary science community and the general public since the gas is recognized as a potential biosignature, due in part to its predominantly biological origin on Earth (Pachauri et al. 2014). Over the past two decades, Mars measurements from a wide variety of platforms (ground-based telescopes, orbiters, and rover) have reported values from zero to ~45 parts per billion by volume (ppbv) that have fueled controversy over the measurements and their subsequent interpretation (Zahnle 2015). Reported measurement examples include ground-based telescope observations from the Canada-France-Hawaii Telescope (CFHT) in 1999 (global average value of 10 ± 3 ppbv (Krasnopolsky et al. 2004) and from the NASA Infrared Telescope Facility (IRTF) in 2003 (Villanueva et al. 2013) (~45 ppbv near the equator), although subsequent ground-based measurements in 2006, 2009, and 2010 found nondetections of methane (Villanueva et al. 2013); and orbital measurements by the Planetary Fourier Spectrometer (PFS) on the Mars Express (MEX) in 2004 and 2010 (Geminale et al. 2011) (global average value of 15 ± 5 ppbv) and in 2019 (Giuranna et al. 2019) (spike of 25 ± 5 ppbv).

The Sample Analysis at Mars (SAM) instrument suite of the Curiosity rover (Mahaffy et al. 2012) has operated successfully on the surface of Mars in Gale crater for over eight years. During this time, the Tunable Laser Spectrometer (TLS-SAM) instrument of the SAM has reported occasional spikes in atmospheric methane (Webster et al. 2015, 2018) up to 20 ppbv (Moores et al. 2019a) detected above a low persistent background level. By enhancing the TLS-SAM sensitivity by a factor of ~25 using the gas processing and atmospheric enrichment of the SAM (Mahaffy et al. 2012; Webster et al. 2018), TLS-SAM discovered that over three Martian years, the low background levels suggest seasonal variation from 0.25 to 0.65 ppbv with a mean value of 0.41 ± 0.16 (95% CI) ppbv for the near-surface methane abundance (Webster et al. 2018). However, Gillen et al. (2020) used statistical analysis to question whether a seasonal cycle was present in the data. Up until December 2019, all the TLS-SAM enrichment measurements were made close to midnight local time on Mars.

* Movie is available at https://www.aanda.org

Table 1. Mars methane spikes reported since the Curiosity landing in 2012.

Instrument	Platform	Date of spike	L_S (deg) [(a)]	CH_4 mixing ratio ppbv ±1 sem	Reference
PFS on Mars Express	Orbiter	Jun. 16 2013	336.12	15.5 ± 2.5	Giuranna et al. (2019)
TLS-SAM on Curiosity	Mars rover	Jun. 16 2013	336.12	5.8 ± 2.3	Webster et al. (2015)
TLS-SAM on Curiosity	Mars rover	Nov. 29 2013–Jan. 28 2014	55.5–81.4	7.2 ± 0.8	Webster et al. (2015)
TLS-SAM on Curiosity	Mars rover	Nov. 22 2016	265.9	5.5 ± 2.1	Webster et al. (2018)
TLS-SAM on Curiosity	Mars rover	Jun. 19 2019	41.5	20.5 ± 2	This paper, in situ value
iSHELL at NASA IRTF	Earth telescope	Jan. 2/9 2017 Jan. 29/31 2018	293 (2017) 122 (2018)	25 ± 1	Novak et al. (2019)

Notes. [(a)]Corresponding to the northern hemisphere (spring equinox at L_S 0°); Curiosity landing site (4.6°S, 137.4°E) is just south of the equator.

Since April 2018, the ESA ExoMars Trace Gas Orbiter (TGO) has been using its Nadir and Occultation for Mars Discovery (NOMAD) (Liuzzi et al. 2019) and Atmospheric Chemistry Suite (ACS) (Korablev et al. 2019) instruments to search for atmospheric methane, but has found none (Montmessin et al. 2020). A comprehensive investigation of Mars methane and organics with NOMAD includes more recent TGO results of continuing nondetection (Knutsen et al. 2021). While both instruments have excellent sensitivity in solar occultation at altitudes above ~3 km, the nadir capability unique to NOMAD has a sensitivity of only ~5 ppbv in the column average, so it would have difficulties to detect even large spikes of methane like the TLS-SAM ~20 ppbv if the spike occurred only within the first kilometer of the surface. TGO has reported (Korablev et al. 2019) a robust nondetection upper limit of ~50 parts per trillion by volume (pptv) of methane in the Martian atmosphere above a few kilometers from the surface over a wide range of latitudes sampled during northern autumn (solar longitudes L_S = 160–240°). If methane is long-lived, and even ignoring the occasional spikes reported by TLS-SAM, it is difficult to reconcile the TGO low upper limit of 50 pptv with the pervasive background measurements of TLS-SAM that average 410 pptv. The concern is one of excess methane buildup over time. Korablev et al. (2019) calculated that if Gale crater were continuously providing 410 pptv that mixed out globally, then this flux of background emission from Gale crater could only have been going on for at most 24 Martian years before the TGO detection limits would be reached. Taking into account the larger spikes of methane reported by TLS-SAM, this 24-yr time frame would be even shorter. It is highly unlikely that methane emissions have been occurring only over the recent decades, and so we are left with an apparent discrepancy between the rover and orbiter data sets.

Using the TGO ACS spectral retrievals near 3.3 μm, Olsen et al. (2020) recently reported detection of 50–200 ppbv ozone in the Martian atmosphere, and suggested that prior methane detections reported by orbiter (Planetary Fourier Spectrometer, PFS), ground-based (telescope) and rover (Curiosity) may all be affected by or attributed to the presence of ozone, not methane, in the Martian atmosphere. In response to this suggestion, Webster et al. (2020) showed that TLS-SAM is of a much higher spectral resolution than all other instruments, including ACS, and in the recorded Martian spectra readily distinguishes methane from ozone lines, the latter not being detected after loss in the instrument's enrichment cell.

Following the first observations of plumes in Martian methane by Mumma et al. (2009), transient spikes in Martian methane have since been reported by several observations (Table 1) since Curiosity landed in 2012. From the Curiosity rover, TLS-SAM recorded three spikes of 5–10 ppbv occurring over the first seven years of operation, the first one on June 15, 2013, of 5.8 ± 2.3 ppbv (Webster et al. 2018). From Mars orbit, using a staring-mode enhancement, the PFS instrument onboard the Mars Express orbiter recently reported (Giuranna et al. 2019) the detection of 15.5 ± 2.5 ppbv on the same date as the first Curiosity spike in June 2013, and over the Gale crater region, the potential source region identified as east of the crater. TLS-SAM reported (Webster et al. 2015, 2018) two additional spikes in the period 2013–16 distinguished over the numerous other measurements at low background levels. More recently, from the Earth, using the NASA IRTF at Maunakea, Hawaii, Novak et al. (2019) reported detection of Mars methane at the 25 ppbv level during January 2017 and January 2018. These detections were consistent with this same group's earlier detections (Novak et al. 2019) of plumes up to 35 ppbv in similar geographic regions.

2. Observations

2.1. New measurements of the diurnal and seasonal variability

The TLS-SAM enrichment measurements and experiment protocol have been described in detail in earlier publications (Webster et al. 2015, 2018) and their supplementary material. The five new measurements presented here were made using exactly the same protocols and instrument run scripts on Mars as earlier measurements. To summarize: After evacuation of the sample (Herriott) cell, the Martian atmosphere is ingested across a molecular sieve material to preferentially remove carbon dioxide and effectively enrich the methane amount (by ~ × 25) in the ~5 mbar cell pressure reached after the two-hour ingest. Then, with the cell closed, the laser scans over the three strong methane lines every second, and on board, TLS captures average spectra over sequential

Table 2. Curiosity TLS-SAM methane enrichment measurements at Gale crater (4.5°S, 137.4°E) over a 70-month period.

Martian sol after landing Aug. 12, 2012	Earth date	Ingest time (LMST)	L_S (deg)	Global pressure multiplier	CH_4 (ppbv)	Error ±1SEM (ppbv)
573.08	17 Mar. 2014	0157	103.48	0.97	0.419	0.089
684.06	9 Jul. 2014	0122	158.61	0.877	0.653	0.121
965.99	25 Apr. 2015	2351	331.57	1.0032	0.609	0.088
1086.06	26 Aug. 2015	0123	32.81	1.05	0.241	0.053
1169.02	19 Nov. 2015	0023	70.57	1.062	0.235	0.076
1322.00	24 Apr. 2016	2355	142.46	0.8808	0.502	0.097
1451.06	4 Sep. 2016	0121	216.58	1.007	0.500	0.078
1527.06	21 Nov. 2016	0130	265.78	1.0765	0.357	0.104
1579.00	13 Jan. 2017	2353	298.76	1.0361	0.246	0.069
1709.00	27 May 2017	0003	10.84	1.0197	0.319	0.098
2076.27	10 Jun. 2018	0121	189.2	0.936	0.474	0.111
2442.16	19 Jun. 2019	0351	41.5	1.064	21.84	0.146
2446.06	23 Jun. 2019	0152	43.3	1.06	0.224	0.123
2615.46	15 Dec. 2019	1120	120.7	0.913	0.067	0.167
2626.99	26 Dec. 2019	2356	126.3	0.90	0.520	0.109
2644.51	12 Jan. 2020	1225	134	0.89	0.036	0.147

Notes. SEM, standard error of the mean; L_S, solar longitude; CI, confidence interval; LMST, local mean standard time. The global pressure multiplier is derived from in situ REMS pressure measurements and is the number by which the original measured in situ values of methane were multiplied to correct the results to the global mean annual mixing ratio given in the last two columns. The in situ values can be found by dividing the last two columns by the global pressure multiplier, and are also given in the appendix tables. The quoted SEM value is calculated from the square root of the sum of the squares of the errors on the individual methane lines (see appendix). Earth date and ingest time refer to the time at which the two-hour gas ingest was started. The enrichment results plotted in Fig. 1 and day/night discussion do not include the large spike observed on sol 2442.16 that is described later.

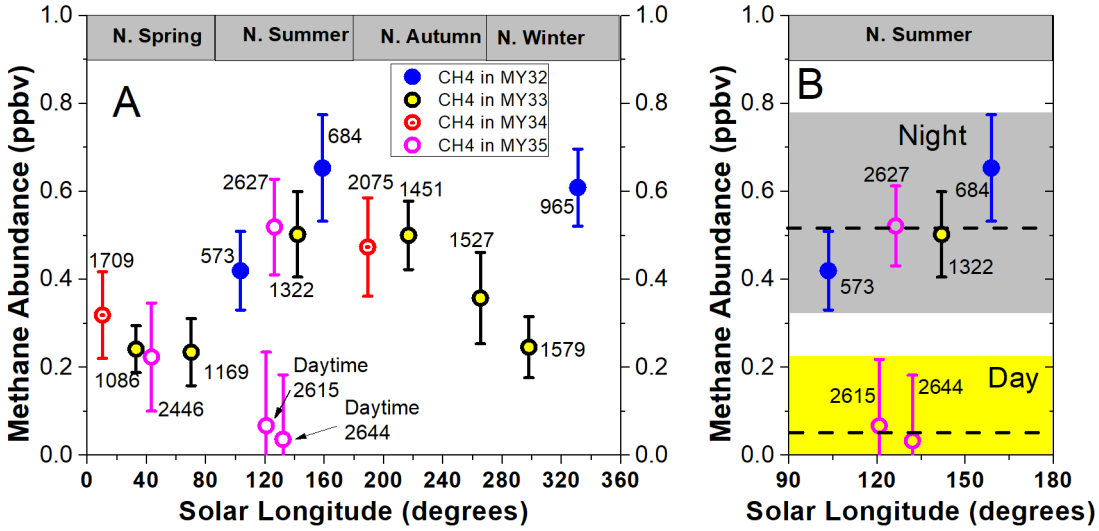

Fig. 1. TLS-SAM enrichment measurements vs. Martian solar longitude. The plotted values have error bars of ±1 SEM, and are corrected to global mean annual values, with these and in situ measured values listed in Table 2. MY, Mars year. (*A*) All enrichment measurement up to January 12, 2020, excluding the 20 ppbv spike seen on June 20, 2019. This plot is an update of one published in Webster et al. (2018), but with five new data points added (whose individual data points are provided in the appendix). (*B*) Subset of the data plotted in (A), in the northern summer time frame, showing a mean value of 0.52 ± 0.10 ppbv (±2SEM) for the five nighttime measurements, and 0.05 ± 0.22 ppbv (±2SEM) for the two daytime measurements. Shaded regions include the full range of the error-bar extremes.

2.7-min periods that are downloaded. Analysis of each of these 2.7-min spectra produces a measurement "point", the process repeated for each of 26 full cell measurements. The cell is then pumped out and an additional 26 "empty cell" spectra are downloaded for analysis (the 52 individual data point values are given in the appendix). All enrichment measurements given in Table 2 result from differencing full and empty-cell measurement mean values.

Table 2 includes a large spike of ~20 ppbv observed on June 2019 that is described in the next section. Figure 1 panel A plots all our enrichment results to date (over a 70-month period), except for the high spike of ~20 ppbv seen in June 2019 that is not considered representative of the background values. Figure 1 panel B expands the northern summer subset of the data to better illustrate the large day-night differences. We highlight the recent MY35 sequence of three runs (day-night-day) taken over a 30-sol

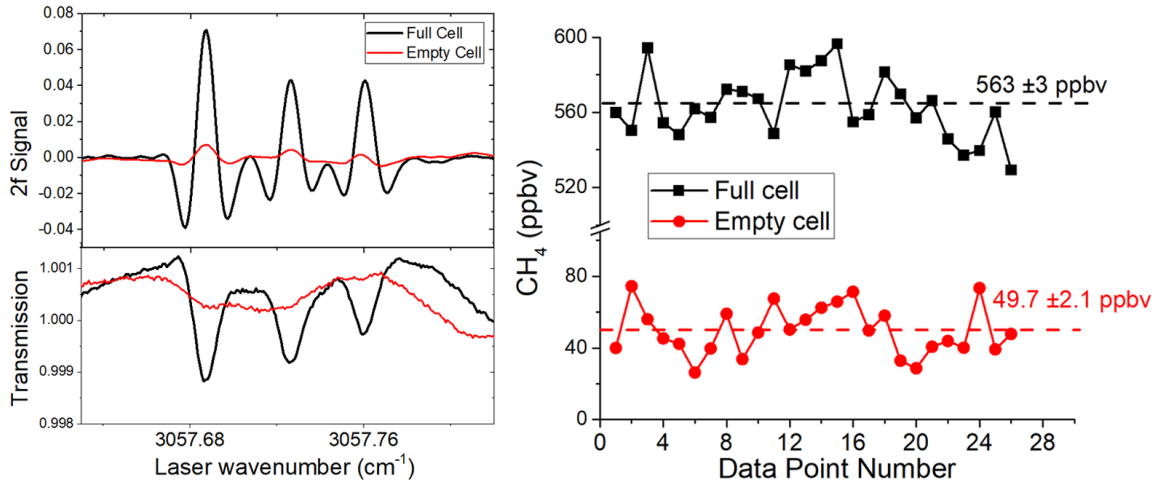

Fig. 2. Spectra and data points for the June 19, 2020, spike in methane. *Left*: actual recorded average for the full cell following the two-hour ingest (black) and a sequential empty cell (red) for comparison. TLS records both direct and second harmonic spectra, the latter providing a better signal-to-noise ratio from a method of high-frequency laser modulation that discriminates against noise and broad interference fringes that are seen in the lower direct absorption spectrum. We note that the direct absorption spectrum analysis produced the same abundance value as the second harmonic result within the quoted errors. *Right*: plots of retrieved in situ CH_4 abundances for each data collection point (26 each for full- and empty-cell runs) as measured in the Herriott cell using 2f spectra comparison with HITRAN 2016 (Gordon et al. 2017). Mean values and standard errors (±1sem) are shown. The reported 20.5 ppbv in situ spike results from taking the difference (full-empty), and dividing by the enrichment factor of 25. Detailed data tables are presented in the appendix.

period. The daytime measurements are the only nondetections that have ever been observed when using the enrichment protocol, while the middle nighttime measurement of 0.52 ppbv falls as expected on the nighttime values that for this season embrace three Mars years.

2.2. Large spike in TLS-SAM atmospheric methane

We report here a new detection of a spike in Mars methane of 20.5 ± 4 (95% CI) ppbv measured in situ in June 2019 that is the highest ever recorded by the Curiosity rover TLS-SAM. When a subsequent measurement was made four days later, this spike had disappeared. It diminished by a factor of 100 to a low background value of 0.22 ppbv.

Figure 2 shows the full- and empty-cell averaged spectra recorded for the June 19, 2019, enrichment run and the individual associated data points. For the spike, the strongest methane spectral line is ~0.2% deep at line center, which HITRAN identifies at our cell temperature and pressure as due to a methane mixing ratio of ~563 ppbv in the cell. Subtracting our empty-cell equivalent value (~50 ppbv) and then dividing the result by our enrichment factor (EF) of 25 (established in test-bed experiments, described in Webster et al. 2018 supplemental material) produces an atmospheric in situ methane value of 20.5 ± 4 ppbv (95% CI), driven predominantly by the error on the EF of 25 ± 4 (95% CI).

The ~20-ppbv spike (Table 1) was seen by TLS-SAM in the pre-dawn hours and is the average value measured during a two-hour gas ingest as the Martian atmospheric pressure drives the flow across the enrichment cell that continuously removes most of the atmospheric carbon dioxide. We did not monitor the methane abundance during the two-hour ingest, and so we cannot tell the temporal shape of the spike, such as whether it was a steady ~20 ppbv value, or included much higher and lower fluctuations during the ingest period. The methane source could have been below the rover and venting upward, or transported horizontally from a near or far location. If transported horizontally, with typical horizontal wind speeds at Gale crater of ~3 m sec^{-1} (Pla-Garcia et al. 2019), a homogeneous ~20-ppbv cloud of methane passing our inlet would therefore be ~20 km in extent for the two-hour ingest. Because we do not resolve the methane abundance versus time over the ingest period, the horizontal extent of a source significantly above background levels could be much smaller or much larger than this.

2.3. Absence of evidence for a rover source of methane

Regarding the assertion by Zahnle (2015) that the rover itself is the source of the Curiosity methane, we agree that in this case, one might expect to see seasonal or diurnal variations that follow the temperature of the rover and its environment. However, working with the MSL team, we have exhausted all efforts to find such a source, as first detailed in the supplemental material in Webster et al. (2018), and to date, no one is able to identify or suggest one. A huge effort by the SAM team to use the extensive housekeeping and other data to verify the pumping and filling protocols and vacuum integrity has found no issues. No dependence is found on the rover inlet orientation with respect to the wind direction, or on the local geology or topography.

The only known rover reservoir of methane is the relatively small amount of terrestrial methane trapped in the TLS foreoptics chamber that amounts to ~10^{15} molecules total. From repeated measurements of the foreoptics pressure and methane content (empty-cell values), and investigating correlations using housekeeping and other data over the eight years of operation, there is no evidence of any significant leakage or change in the foreoptics methane amount (except on very few occasions when we deliberately pumped out the chamber to lower pressures). Over the eight years of operation on Mars, and up to the latest measurement reported here, the foreoptics methane amount remains between ~1–2 nanomoles as measured for the data presented here, which is identical to the last value reported in the data plots in the supplemental material of Webster et al. (2018).

There is not enough methane in the foreoptics to explain the large amounts seen during spike observations, even if all the methane were to be available. For example, if we consider a 1m diameter cross-section of Martian air moving across our external inlet during the two-hour ingest period, even at a lower Mars wind speed of 1 m sec^{-1}, it would be 7.2 km long, and sweep out a cylindrical volume of ~5600 m^3. For the large spike reported here, with an average volume mixing ratio of 20 ppbv at 7 mbar pressure, this would contain $\sim 2 \times 10^{19}$ molecules of methane, or about 20 000 times the total number of methane molecules contained in the foreoptics chamber. By comparison, background levels of ~0.4 ppbv would also exceed the available foreoptics content by a factor of ~400. In the absence of any other identified or suggested rover source, we therefore identify this ~20 ppbv spike and all other TLS-SAM measurements of methane as Martian in origin and not generated by the rover.

3. Discussion and conclusions

A critical issue is to understand to what extent the nighttime measurements at Gale crater are representative of the methane flux over the whole day at Gale crater and other near-surface locations because day-night differences in the TLS-SAM measurements have the potential to identify the mechanisms at play and to reduce the discrepancy between the Curiosity and ExoMars TGO data sets (Moores et al. 2019a). Numerous mechanisms for Martian methane production and emission have been proposed to date (e.g., Yung et al. 2018, and references therein). However, methane origin by these processes does not explain either the suggested seasonal variation of methane or the methane spikes detected by Curiosity.

Seasonal variation in the methane background levels suggested by the TLS-SAM background data (Webster et al. 2018) has been reproduced to some extent by the one-dimensional numerical model of Moores et al. (2019b) based on temperature-dependent emissions, and by Viúdez-Moreiras et al. (2019) based on wind-dependent emissions. In the first scenario, the model of Moores et al. (2019b) is based on methane adsorption onto and diffusion through the regolith, although methane destruction had a timescale that was a free parameter and methane thermodynamic absorption differed from laboratory-based parameters. With these constraints, the regolith was assumed to be impregnated with methane from earlier plume events or supplied from the underlying surface by microseepage (Etiope & Oehler 2019). Since that study, the very low upper limits on higher altitude methane provided by TGO provide tighter constraints on the calculated magnitude of microseepage that are included in updated modeling calculations by the Moores' group (Moores et al. 2019a) that demonstrates that diurnal variation needs to be considered. This group proposed that the TLS-SAM measurements could be partly reconciled with those of TGO by the inhibition of mixing near the surface overnight whereby methane emitted from the subsurface accumulates within meters of the surface before being mixed below detection limits shortly after dawn. This nighttime accumulation and inhibition of mixing to higher altitudes is enabled by the collapse of the planetary boundary layer (PBL) from many kilometers during the day to only meters at night (Guzewich et al. 2017).

Pla-Garcia et al. (2019) explored the suppression of mixing by modeling the dynamics near Gale crater in three dimensions with the Mars Regional Atmospheric Modeling System (MRAMS; Rafkin & Michaels 2019). The results from the most relevant MRAMS scenarios are shown in Fig. 3 below, and in

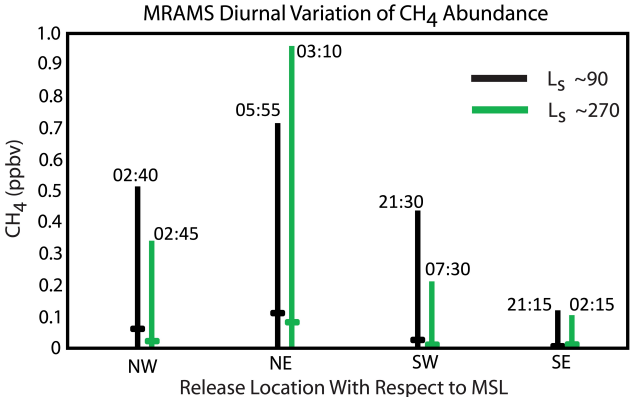

Fig. 3. Diurnal variations of the methane mixing ratio for two seasons calculated from the Mars Regional Atmospheric Modeling System sampled at the Curiosity rover location for sol 305 assuming a constant methane surface flux of 1.8×10^{-6} kg m^{-2} s^{-1} emanating from locations ~1 grid point (2.96 km) to the NE, SE, SW, and NW of the rover. Vertical bars represent the amplitude of the diurnal cycle. The average local time of maximum abundance is indicated in the label at the top of the vertical bars. Thick horizontal lines indicate the diurnally averaged value.

Figs. A.1 and A.2 at solar longitude values of L_S 90° and L_S 270°. The selection of L_S 270° is based on its identification as an anomalous very windy season with large amplitude breaking mountain waves, and rapid mixing with air external to the crater. Outside of the L_S 270° season, mixing between the crater air mass and the external crater air was interpreted to be more subdued. L_S 270° was selected as being representative of "most of the year" for mixing experiments. All MRAMS simulations produce a strong diurnal cycle in the modeled methane abundance, with variations spanning an order of magnitude or more on the order of several hours, increasing during the evening and night, and decreasing during the daytime, as shown in the figures. The methane abundance tends to increase overnight when the PBL is shallow and the downslope, convergent circulations locally confine the surface release. The methane abundance tends to decrease during the day when the PBL grows (Moores et al. 2019b) and divergent, upslope circulations transport methane away from the release area (Pla-Garcia et al. 2019). Animations of the diurnally varying circulation and methane abundance from MRAMS are provided in the appendix. The MRAMS model emphasizes the importance of location of release and horizontal transport in addition to PBL vertical mixing.

Most of the time, the average value is well below the peak (i.e., the peaks are relatively short-lived). The mean values and range of values show that the modeled values depend on location of release, time of day, and season and represent the importance of vertical PBL mixing and horizontal transport, both of which act to determine the local time and magnitude of the peak methane abundance. A release location to the NE produces the highest values, while a location to SE (from Aeolis Mons) produces the lowest. The dependence on direction is due to the prevailing wind. If we assume that micro-seepage is responsible for the methane detected at Gale crater, the Moores et al. (2019a) model allows micro-seepage fluxes at Gale to be derived, consistent with a constant 1.5×10^{-10} kg m^{-2} sol^{-1} (5.4×10^{-5} tonnes km^{-2} yr^{-1}) source at depth that is an order of magnitude lower than that required to produce the Curiosity measurements if the methane abundance does not exhibit diurnal variation. However, the constraints of the TGO results (Korablev et al. 2019) combined with the assumption that methane retains its

~300-yr lifetime implied that a surface area of only ~1.5 times that of the Gale crater region could be emitting methane, unless a fast destruction mechanism exists. Under this scenario, the model of Moores et al. (2019a) predicted that daytime TLS-SAM measurements should be close to zero, as reported in this paper.

The release of methane to the atmosphere by means of seepage should also be strongly affected by winds and pressure fluctuations. Model simulations suggest that advective fluxes produced by winds have strong relevance on regolith emissions under Martian conditions in highly permeable soils such as fracture media (Viúdez-Moreiras et al. 2020). A potential seasonal variation in the methane background levels is also indicated by a numerical model considering wind-dependent methane emissions in Aeolis Mons and in other crater locations (Viúdez-Moreiras et al. 2020). MSL data showed evidence of a correlation between the seasonal cycle of surface wind speeds as measured by REMS and the seasonal variation of methane abundance detected by TLS-SAM, pointing to a local source of methane responsible for the background seasonal variation reported by SAM. The temperature- and wind-dependent emission mechanisms are compatible and could be regulating methane emissions constructively.

Because there exist numerous other areas of similar geological features to Gale crater, Etiope & Oehler (2019) argued that a small emitting area of Mars is unrealistic, and that a fast destruction or sequestration mechanism is necessary to avoid the problem of excess methane building up in the Martian atmosphere above the levels observed by TGO. By effectively decreasing the lifetime of methane in the Martian atmosphere, a fast destruction (e.g., Atreya et al. 2011; Delory et al. 2006) or sequestration process (e.g., Jensen et al. 2014) would allow a substantially larger area to be emitting methane than that calculated by Moores et al. (2019a).

The TLS-SAM results show that a fast destruction or sequestration of methane is required (Korablev et al. 2019; Etiope & Oehler 2019), unless Gale crater is the only source of methane (Moores et al. 2019a), which is unlikely. Several mechanisms for fast destruction of methane have been proposed in the past, including energetic electrons resulting from triboelectric process during convective dust events (Farrell et al. 2006), and, globally, CH_4 sequestration on airborne dust (Jensen et al. 2014), and superoxides from hydrogen peroxide in the surface/subsurface (Delory et al. 2006; Atreya et al. 2006, 2011, 2019). The hypotheses of fast destruction of methane require further modeling and laboratory studies under appropriate environmental and geochemical conditions to assess their quantitative validity for Mars.

The daytime absence of methane recorded by TLS-SAM, and the new additional nighttime values reported here, are a critical update to the Curiosity data set to constrain the possible mechanisms of methane production and removal on Mars and are a step toward reconciling the apparent differences between this data set and that of the TGO. Building upon the models of Moores et al. (2019b,a), Viúdez-Moreiras et al. (2020), Pla-Garcia et al. (2019), and of Etiope & Oehler (2019), the TLS-SAM data provide evidence for methane production from a near-surface source, most likely from continuous micro-seepage, that is temporarily contained in the near-surface atmosphere during the night due to the low planetary boundary layer, reduced atmospheric mixing, and horizontal transport. Increased atmospheric dynamics during the daytime mixes the gas accumulated in the night into the global atmosphere where it is diluted to the very low levels constrained by the TGO nondetection. We consider it highly unlikely that Gale crater is the only source area of micro-seepage, and therefore for the scenario implied by the Curiosity measurements, a fast methane destruction or sequestration mechanism must be occurring in the lower atmosphere of Mars as discussed above.

Acknowledgements. The research described here was carried out in part at the Jet Propulsion Laboratory, California Institute of Technology, under a contract with the National Aeronautics and Space Administration (NASA). Funding: funding from NASA's Planetary Science Division is acknowledged by authors C.W., P.M., S.A., G.F., C.M., S.T., S.R., A.V. D.V.M. and J.P.G. acknowledge funding from Centro de Astrobiología (CAB, CSIC-INTA), under contract ESP2016-79612-C3-1-R. J.M., H.K. and C.S. acknowledge funding from the Canadian Space Agency MSL participating scientist program. J.P.G. acknowledges additional funding from the Spanish Ministry of Economy and Competitiveness under contract ESP2016-79612-C3-1-R. Author contributions: C.W., P.M. = TLS-SAM Instrument design, build and testing (IDBT), surface operations (SO), test-bed activities (TBA), data analysis (DA), data correlations (DC), science interpretation (SI). G.F., C.M. = IDBT, SO, TBA, D.A.; S.A., J.M., H.K., C.S., D.V.M., J.P.G., S.R., A.V. = SI, DC; S.T. = SO. Competing interests: no potential conflicts of interest exist for any of the listed authors. Data and materials availability: data described in the paper are publicly-available from NASA's Planetary Data System (PDS) under an arrangement with the Mars Science Laboratory (MSL) project. URL of SAM page at PDS is `http://pds-geosciences.wustl.edu/missions/msl/sam.htm`.

References

Atreya, S. K., Wong, A.-S., Renno, N. O., et al. 2006, Astrobiology, 6, 439
Atreya, S. K., Witasse, O., Chevrier, V. F., et al. 2011, Planet. Space Sci., 59, 133
Atreya, S. K., Encrenaz, T., Korablev, O., et al. 2019, in Ninth International Conference on Mars, eds. D. W. Beaty, B. Carrier, S. Diniega, B. Ehlmann, R. W. Zurek, et al. (Pasadena, California: Lunar and Planetary Institute)
Delory, G. T., Farrell, W. M., Atreya, S. K., et al. 2006, Astrobiology, 6, 451
Etiope, G., & Oehler, D. Z. 2019, Planet. Space Sci., 168, 52
Farrell, W., Delory, G., & Atreya, S. 2006, Geophys. Res. Letters, 33, 21
Geminale, A., Formisano, V., & Sindoni, G. 2011, Planet. Space Sci., 59, 137
Gillen, E., Rimmer, P. B., & Catling, D. C. 2020, Icarus, 336, 113407
Giuranna, M., Viscardy, S., Daerden, F., et al. 2019, Nat. Geosci., 12, 326
Gordon, I. E., Rothman, L. S., Hill, C., et al. 2017, J. Quant. Spectr. Rad. Transf., 203, 3
Guzewich, S. D., Newman, C., Smith, M., et al. 2017, J. Geophys. Res. Planets, 122, 2779
Jensen, S. J. K., Skibsted, J., Jakobsen, H. J., et al. 2014, Icarus, 236, 24
Knutsen, E. W., Villanueva, G. L., Liuzzi, G., et al. 2021, Icarus, 357, 114266
Korablev, O., Vandaele, A. C., Montmessin, F., et al. 2019, Nature, 568, 517
Krasnopolsky, V. A., Maillard, J. P., & Owen, T. C. 2004, Icarus, 172, 537
Liuzzi, G., Villanueva, G. L., Mumma, M. J., et al. 2019, Icarus, 321, 671
Mahaffy, P. R., Webster, C. R., Cabane, M., et al. 2012, Space Sci. Rev., 170, 401
Montmessin, F., Korablev, O., Fedorova, A. A., et al. 2020, in European Planetary Science Congress, EPSC2020–637
Moores, J. E., Gough, R. V., Martinez, G. M., et al. 2019a, Nat. Geosci., 12, 321
Moores, J. E., King, P. L., Smith, C. L., et al. 2019b, Geophys. Res. Lett., 46, 9430
Mumma, M. J., Villanueva, G. L., Novak, R. E., et al. 2009, Science, 323, 1041
Novak, R. E., Mumma, M. J., Villanueva, G. L., & Faggi, S. 2019, in Ninth International Conference on Mars, eds. D. W. Beaty, B. Carrier, S. Diniega, B. Ehlmann, R. W. Zurek, et al. (Pasadena, California: Lunar and Planetary Institute)
Olsen, K. S., Lefèvre, F., Montmessin, F., et al. 2020, A&A, 639, A141
Pachauri, R. K., Allen, M. R., Barros, V. R., et al. 2014, Climate change 2014: synthesis report. Contribution of Working Groups I, II and III to the fifth assessment report of the Intergovernmental Panel on Climate Change (Geneva, Switzerland: Ipcc)
Pla-Garcia, J., Rafkin, S. C., Karatekin, Ö., & Gloesener, E. 2019, J. Geophys. Res. Planets, 124, 2141
Rafkin, S., & Michaels, T. 2019, Atmosphere, 10, 747
Villanueva, G., Mumma, M., Novak, R., et al. 2013, Icarus, 223, 11
Viúdez-Moreiras, D., Gómez-Elvira, J., Webster, C., et al. 2019, in Fall Meeting American Geophysical Union, AGU, San Francisco, CA, USA
Viúdez-Moreiras, D., Arvidson, R., Gómez-Elvira, J., et al. 2020, Geophys. Res. Lett., 47, e2019GL085694
Webster, C. R., Mahaffy, P. R., Atreya, S. K., et al. 2015, Science, 347, 415
Webster, C. R., Mahaffy, P. R., Atreya, S. K., et al. 2018, Science, 360, 1093
Webster, C. R., Mahaffy, P. R., Atreya, S. K., et al. 2020, A&A, 641, L3
Yung, Y. L., Chen, P., Nealson, K., et al. 2018, Astrobiology, 18, 1221
Zahnle, K. 2015, Science, 347, 370

Appendix A: MRAMS simulations

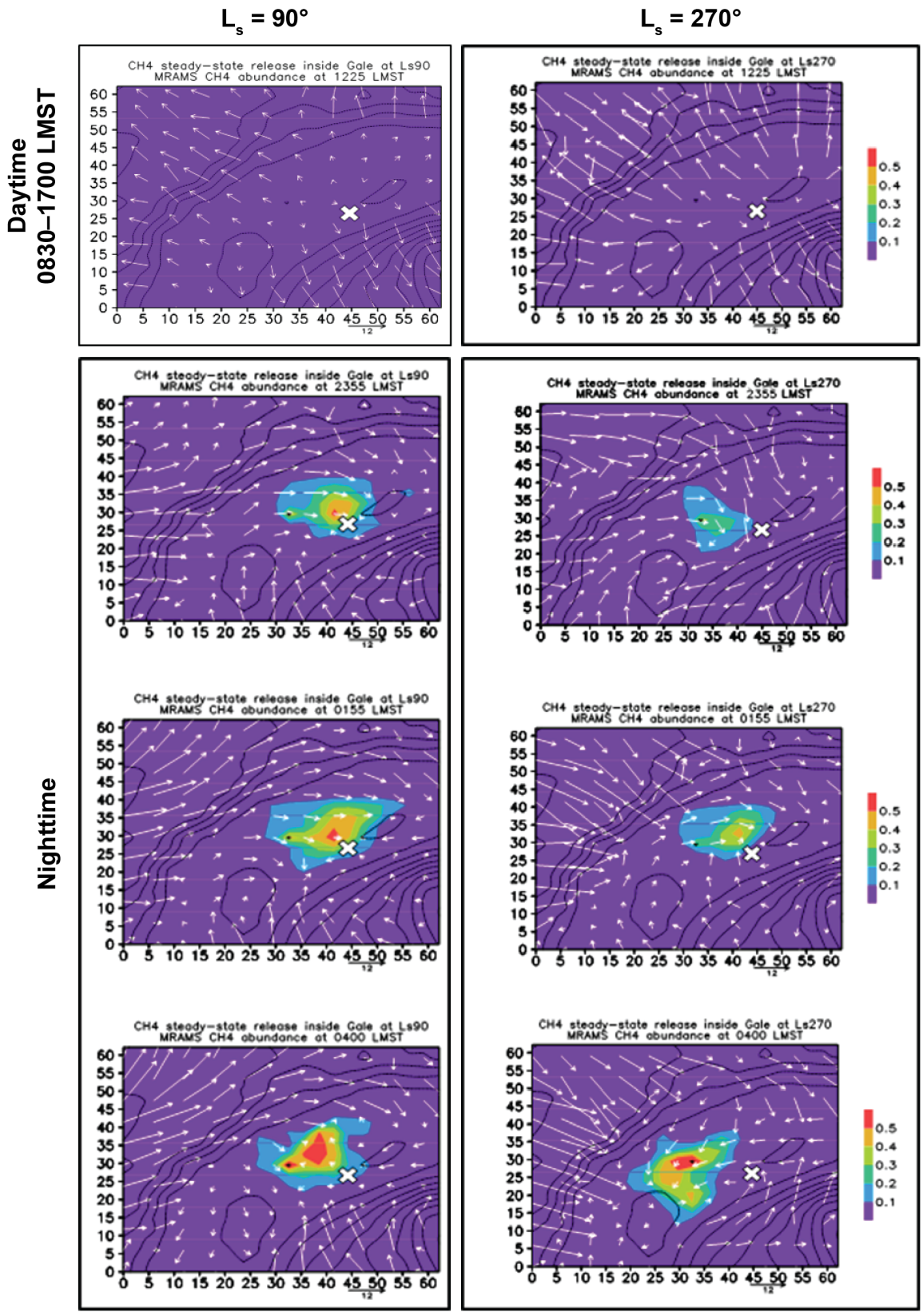

Fig. A.1. Plan view of the NW quadrant of Gale crater with a methane mixing ratio in the lowest model layer for a time series of steady-state methane release at L_S 90° and L_S 270° ~1 grid point (2.96 km) NW of the Curiosity rover location for sol 305, which is marked with a white cross. Methane is emitted continuously (steady-state release) from the surface at a flux of 1.8×10^{-6} kg m^{-2} s^{-1}. The methane mixing ratio from 0830 to 1700 is zero. White arrows represent the wind speed and direction. Black contours represent the topography. The methane steady-state release began at 0500 LMST on the sol before. The *x*-*y* axis labels distance in km. The color scale shows ppbv CH_4.

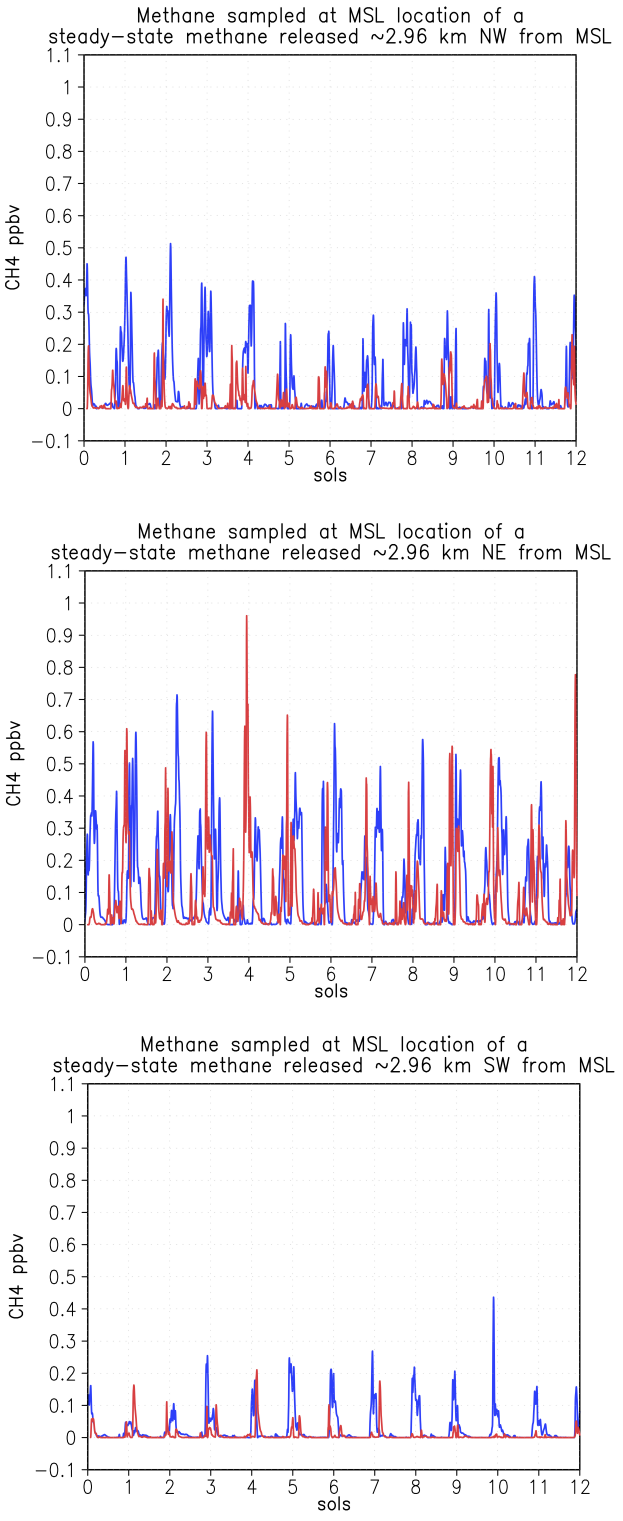

Fig. A.2. Twelve-sol time series of the MRAMS methane abundances sampled at the Curiosity rover location for sol 305 for three steady-state released inside Gale crater ~1 grid point (2.96 km) km NW, NE, and SW from rover location, each with an area of ~150 km^2. Blue is L_S 90°, and red is L_S 270°. The abundance of tracers is shown shortly after the flux is turned on. Integer values of sols correspond to midnight, and intermediate values (0.5, 1.5, etc.) correspond to noon.

MRAMS animations are available online. Gale crater plan view diurnal cycle animation of winds and methane abundance evolution in the lowest model layer for a steady-state methane release at L_S 90° ~ 1 grid point (2.96 km) NW of the Curiosity rover location on sol 305. White arrows represent the wind speed and direction. Black contours represent the topography. "CH_4 detected" means "Modeled CH_4 abundance". Hours in LMST are shown in the upper right corner and methane values are given in ppbv. White arrows represent the wind speed and direction. The *x*-*y* axis labels distance in grid points (each of 2.96 km).

Appendix B: TLS-SAM data

Columns are:

Index	Sequential data points, each resulting from on-board averaging of spectra for ~2.7 min
Elapsed time	s
Foreoptics pressure	mbar
Laser plate temp	°C
Foreoptics temp	°C
Ref cell temp	°C
Science detector temp	°C
HCell pressure	mbar
e line in situ CH_4	ppbv
f line in situ CH_4	ppbv
g line in situ CH_4	ppbv
Wefg in situ CH_4	ppbv – mean value (e+f+2g)/4

Table B.1. TLS-SAM data.

Index	Elapsed time	Foreoptics pressure	Laser plate temp	Foreoptics temp	Ref cell temp	Science detector temp	HCell pressure	e line in situ CH_4 ppbv	f line in situ CH_4 ppbv	g line in situ CH_4 ppbv	Wefg in situ CH_4 ppbv
Sol 2442.16 Full Cell:											
1	12 287	4.038	16.5	44.513	42.955	47.162	5.423	581.195	537.89	560.019	559.781
2	12 447	4.028	16.351	44.887	42.642	46.648	5.194	579.665	516.427	552.75	550.398
3	12 611	4.035	16.252	44.585	42.978	47.246	5.442	624.898	570.047	591.133	594.303
4	12 775	4.05	16.185	44.033	42.48	46.361	5.203	561.093	595.578	530.559	554.448
5	12 940	4.066	16.14	44.756	42.96	47.3	5.445	510.366	587.251	547.335	548.072
6	13 104	4.047	16.117	43.718	42.524	46.469	5.21	583.76	564.155	549.804	561.881
7	13 268	4.078	16.094	44.954	42.937	47.336	5.371	561.813	584.361	541.307	557.197
8	13 433	4.112	16.086	43.892	42.605	46.653	5.278	578.877	566.803	571.784	572.312
9	13 597	4.09	16.08	45.006	42.998	47.428	5.439	545.139	559.521	589.881	571.106
10	13 762	4.115	16.076	43.941	42.656	46.728	5.293	592.391	566.178	555.179	567.232
11	13 926	4.078	16.08	45.203	42.902	47.282	5.318	565.389	567.036	531.103	548.658
12	14 090	4.118	16.081	44.092	42.711	46.863	5.346	603.034	547.432	595.284	585.259
13	14 249	4.094	16.093	45.329	42.653	46.874	5.2	624.243	578.232	562.935	582.086
14	14 414	4.143	16.11	44.291	42.781	47.022	5.405	586.892	594.098	584.322	587.409
15	14 578	4.143	16.124	45.415	42.742	47.019	5.256	615.477	593.685	588.483	596.532
16	14 742	4.131	16.145	44.356	42.847	47.114	5.414	576.536	542.663	550.26	554.93
17	14 907	4.137	16.16	44.729	42.498	46.543	5.175	599.087	563.224	536.276	558.716
18	15 071	4.162	16.198	44.522	42.867	47.203	5.448	612.257	559.297	576.844	581.311
19	15 236	4.14	16.182	43.999	42.409	46.347	5.203	578.164	569.71	565.659	569.798
20	15 400	4.165	16.188	44.717	42.905	47.288	5.461	534.848	545.006	574.09	557.009
21	15 564	4.131	16.196	43.708	42.495	46.476	5.222	544.441	580.147	570.121	566.207
22	15 729	4.177	16.198	44.935	42.913	47.326	5.42	492.984	587.609	551.296	545.796
23	15 893	4.162	16.199	43.892	42.599	46.659	5.287	501.89	535.954	555.475	537.199
24	16 057	4.128	16.198	45.165	42.87	47.25	5.318	494.316	538.439	562.926	539.652
25	16 222	4.156	16.198	44.067	42.685	46.826	5.352	561.679	569.701	554.453	560.071
26	16 386	4.156	16.196	45.272	42.963	47.383	5.361	468.362	513.465	567.745	529.329
Sol 2442.16 Empty cell:											
1	17 612	4.18	16.267	44.108	42.708	46.849	0.054	11.996	65.557	41.124	39.951
2	17 776	4.171	16.244	45.307	42.862	47.201	−0.067	74.484	59.965	80.329	74.484
3	17 935	4.193	16.222	44.198	42.771	46.956	0.063	55.976	40.796	61.376	55.976
4	18 099	4.165	16.205	45.368	42.864	47.201	−0.101	45.307	42.517	62.585	45.307
5	18 264	4.152	16.185	44.203	42.781	46.979	0.039	42.247	68.089	35.177	42.247
6	18 428	4.18	16.175	45.197	43.057	47.513	0.042	26.216	41.646	49.774	26.216
7	18 593	4.193	16.162	44.082	42.762	46.908	−0.014	39.679	54.653	69.193	39.679
8	18 757	4.168	16.152	45.182	43.01	47.446	−0.02	59.002	57.484	79.531	59.002
9	18 921	4.165	16.145	44.057	42.736	46.886	−0.033	33.659	43.823	31.204	33.659
10	19 085	4.156	16.145	45.189	42.983	47.426	−0.042	48.574	30.273	48.414	48.574
11	19 250	4.149	16.157	44.051	42.726	46.892	−0.048	67.555	31.561	78.44	67.555
12	19 414	4.128	16.182	45.203	42.967	47.417	−0.07	50.244	24.264	68.685	50.244
13	19 578	4.14	16.208	44.055	42.719	46.903	−0.057	55.748	71.454	49.767	55.748
14	19 738	4.143	16.229	45.071	43.077	47.585	0.051	62.461	53.936	81.922	62.461
15	19 902	4.118	16.255	43.961	42.703	46.84	−0.088	65.84	47.338	80.106	65.84
16	20 066	4.112	16.274	45.057	43.039	47.522	0.005	71.331	65.795	75.732	71.331
17	20 230	4.131	16.295	43.948	42.683	46.849	0.005	49.711	87.982	50.933	49.711
18	20 395	4.118	16.318	45.035	43.012	47.488	−0.008	58.067	64.915	61.441	58.067
19	20 559	4.121	16.343	43.922	42.658	46.792	−0.107	32.826	24.825	40.286	32.826
20	20 724	4.1	16.366	45.038	42.993	47.479	−0.061	28.591	−2.558	37.718	28.591
21	20 888	4.143	16.389	44.04	42.65	46.79	−0.11	40.667	53.093	38.936	40.667
22	21 053	4.109	16.414	44.9	43.069	47.56	0.06	43.862	44.448	39.888	43.862
23	21 217	4.081	16.442	43.905	42.625	46.699	−0.157	40.095	9.437	49.408	40.095
24	21 381	4.09	16.47	44.864	43.034	47.497	0.032	73.454	58.659	71.016	73.454
25	21 540	4.078	16.496	44.523	42.661	46.799	−0.163	39.176	23.678	46.978	39.176
26	21 704	4.072	16.526	44.741	43.07	47.613	0.06	47.795	46.373	51.797	47.795

Table B.1. continued.

Index	Elapsed time	Foreoptics pressure	Laser plate temp	Foreoptics temp	Ref cell temp	Science detector temp	HCell pressure	e line in situ CH_4 ppbv	f line in situ CH_4 ppbv	g line in situ CH_4 ppbv	Wefg in situ CH_4 ppbv
Sol 2446.06 Full Cell:											
1	12 228	4.069	17.061	45.208	43.414	47.216	5.513	74.386	49.673	81.6	71.815
2	12 388	4.078	16.877	44.266	43.067	46.54	5.281	69.75	94.44	73.876	77.986
3	12 552	4.094	16.744	45.493	43.373	47.219	5.43	42.808	57.897	40.566	45.459
4	12 712	4.121	16.655	44.476	43.154	46.78	5.433	52.445	34.922	50.479	47.081
5	12 876	4.069	16.591	45.738	43.193	46.972	5.318	58.646	97.676	49.557	63.859
6	13 035	4.097	16.549	44.672	43.223	46.969	5.473	60.601	59.286	43.795	51.869
7	13 195	4.125	16.525	45.113	42.902	46.469	5.275	31.861	31.235	60.062	45.805
8	13 354	4.137	16.502	44.88	43.27	47.123	5.532	51.127	27.893	68.241	53.876
9	13 519	4.134	16.486	44.215	42.809	46.299	5.303	62.655	29.937	52.431	49.363
10	13 678	4.146	16.478	45.118	43.299	47.243	5.541	78.156	71.141	26.48	50.564
11	13 837	4.177	16.465	44.177	42.947	46.541	5.358	−25.196	36.323	43.499	24.531
12	14 002	4.168	16.463	45.368	43.302	47.275	5.482	99.638	39.389	74.299	71.906
13	14 161	4.159	16.459	44.389	43.062	46.763	5.423	96.247	5.363	23.77	37.288
14	14 325	4.168	16.46	45.641	43.193	47.101	5.352	106.794	55.575	52.821	67.003
15	14 485	4.193	16.459	44.59	43.156	46.954	5.489	83.986	61.745	26.067	49.466
16	14 649	4.168	16.463	45.409	42.948	46.66	5.275	54.121	27.484	49.376	45.089
17	14 814	4.187	16.462	44.77	43.223	47.097	5.52	87.546	32.29	32.6	46.259
18	14 979	4.193	16.46	44.713	42.815	46.389	5.293	40.899	54.379	36.013	41.826
19	15 138	4.152	16.465	44.978	43.257	47.225	5.544	116.006	46.442	59.624	70.424
20	15 298	4.221	16.465	44.067	42.877	46.453	5.327	78.077	62.485	53.31	61.795
21	15 462	4.202	16.46	45.355	43.181	47.126	5.414	55.086	58.308	41.304	49.001
22	15 622	4.214	16.46	44.363	43	46.73	5.43	93.194	72.199	44.623	63.66
23	15 786	4.187	16.46	45.657	43.059	46.928	5.318	88.757	79.31	68.531	76.282
24	15 945	4.224	16.457	44.612	43.127	46.963	5.489	118.218	81.801	58.315	79.163
25	16 105	4.199	16.45	45.038	42.827	46.465	5.265	57.507	64.094	72.061	66.431
26	16 264	4.211	16.446	44.899	43.243	47.184	5.547	87.317	16.249	68.38	60.081
Sol 2446.06 Empty cell:											
1	17 486	4.211	16.46	44.103	42.867	46.479	0.017	37.222	83.257	26.137	43.188
2	17 650	4.211	16.423	45.277	43.178	47.14	0.073	56.083	35.57	62.943	56.083
3	17 810	4.106	16.383	44.285	42.952	46.662	0.067	64.098	88.094	70.942	64.098
4	17 974	4.205	16.356	45.39	43.242	47.243	0.082	59.023	67.254	69.546	59.023
5	18 139	4.205	16.321	44.344	43.015	46.774	0.104	59.556	101.011	55.525	59.556
6	18 303	4.19	16.29	45.451	43.284	47.309	0.06	44.561	58.278	39.669	44.561
7	18 467	4.211	16.262	44.394	43.06	46.829	0.07	73.352	92.15	67.522	73.352
8	18 626	4.165	16.241	45.613	43.044	46.92	−0.129	66.534	77.027	64.289	66.534
9	18 791	4.196	16.225	44.537	43.089	46.944	0.085	79.758	52.992	91.933	79.758
10	18 950	4.171	16.209	45.622	43.042	46.933	−0.116	47.715	52.361	47.065	47.715
11	19 114	4.168	16.196	44.6	43.134	47.026	0.095	40.315	41.629	49.171	40.315
12	19 279	4.152	16.19	45.64	43.054	46.954	−0.123	28.599	49.56	35.899	28.599
13	19 443	4.159	16.186	44.626	43.156	47.069	0.095	35.891	30.525	39.772	35.891
14	19 607	4.156	16.18	45.633	43.059	46.967	−0.123	48.591	67.339	40.789	48.591
15	19 767	4.152	16.172	44.664	43.173	47.108	0.101	32.756	33.874	43.855	32.756
16	19 931	4.128	16.17	45.577	43.01	46.838	−0.15	39.933	58.409	49.981	39.933
17	20 090	4.156	16.163	44.718	43.198	47.166	0.116	41.563	48.422	50.728	41.563
18	20 254	4.134	16.157	45.442	42.98	46.826	−0.16	47.137	43.821	55.838	47.137
19	20 419	4.137	16.152	44.732	43.208	47.18	0.107	51.479	44.534	61.386	51.479
20	20 583	4.115	16.145	45.418	42.973	46.82	−0.169	60.194	71.456	55.325	60.194
21	20 747	4.131	16.132	44.741	43.206	47.191	0.101	61.525	71.105	61.373	61.525
22	20 906	4.115	16.122	45.269	42.938	46.747	−0.166	49.621	51.021	35.614	49.621
23	21 071	4.134	16.11	44.76	43.213	47.207	0.104	31.908	28.34	35.266	31.908
24	21 230	4.125	16.099	45.106	42.89	46.671	−0.169	59.626	43.366	55.183	59.626
25	21 394	4.115	16.091	44.79	43.215	47.223	0.107	49.955	15.35	55.152	49.955
26	21 559	4.1	16.087	45.064	42.87	46.646	−0.172	57.6	71.708	37.696	57.6

Table B.1. continued.

Index	Elapsed time	Foreoptics pressure	Laser plate temp	Foreoptics temp	Ref cell temp	Science detector temp	HCell pressure	e line in situ CH_4 ppbv	f line in situ CH_4 ppbv	g line in situ CH_4 ppbv	Wefg in situ CH_4 ppbv
Sol 2615.46 Full Cell:											
1	11 981	5.334	27.357	46.049	43.904	46.547	4.283	135.479	17.269	28.197	52.285
2	12 291	5.377	26.993	44.631	43.912	46.281	4.351	104.252	73.575	26.428	57.671
3	12 455	5.383	26.891	45.69	44.142	46.755	4.376	48.731	64.156	54.774	55.609
4	12 615	5.417	26.829	44.95	44.065	46.529	4.453	31.583	25.387	57.374	42.929
5	12 779	5.408	26.801	44.528	43.693	45.869	4.258	15.087	91.366	45.061	49.144
6	12 939	5.365	26.856	45.689	44.394	47.006	4.574	39.8	35.839	63.341	50.581
7	13 103	5.454	26.794	44.973	44.133	46.531	4.456	27.345	5.976	−1.723	7.469
8	13 268	5.454	26.819	44.797	43.751	45.897	4.28	77.348	62.378	89.491	79.677
9	13 432	5.482	26.847	45.34	44.198	46.719	4.531	52.422	48.906	49.173	49.918
10	13 597	5.479	26.883	44.677	43.931	46.172	4.363	37.868	24.694	26.082	28.682
11	13 761	5.476	26.921	46.161	44.14	46.651	4.342	86.652	39.324	61.217	62.102
12	13 920	5.538	26.958	45.368	44.317	46.838	4.596	122.559	42.634	51.856	67.227
13	14 080	5.523	26.991	44.748	44.023	46.244	4.369	36.618	103.145	51.267	60.574
14	14 244	5.52	27.017	45.875	43.938	46.228	4.264	79.918	47.477	60.533	62.115
15	14 403	5.544	27.039	45.159	44.159	46.566	4.509	42.793	13.494	36.844	32.494
16	14 563	5.541	27.068	44.561	43.863	46.001	4.323	72.918	65.321	30.767	49.944
17	14 727	5.551	27.087	45.964	44.324	46.91	4.5	72.567	99.462	44.13	65.072
18	14 887	5.56	27.106	45.331	44.295	46.735	4.506	186.899	62.761	71.12	97.975
19	15 051	5.563	27.124	44.706	43.963	46.152	4.314	86.857	37.665	65.14	63.7
20	15 215	5.594	27.141	45.743	44.198	46.628	4.422	59.187	115.704	71.03	79.238
21	15 375	5.582	27.155	45.047	44.15	46.47	4.49	76.214	132.542	46.226	75.302
22	15 539	5.585	27.168	44.653	43.815	45.875	4.32	76.857	73.998	40.859	58.143
23	15 698	5.613	27.173	45.53	44.283	46.785	4.574	3.319	110.778	10.901	33.975
24	15 863	5.6	27.178	44.845	44.065	46.274	4.425	56.336	50.103	70.789	62.004
25	16 028	5.594	27.176	45.589	43.866	46.017	4.289	19.821	14.399	35.624	26.367
26	16 192	5.619	27.172	45.57	44.399	46.91	4.645	78.805	90.184	55.07	69.782
Sol 2615.46 Empty cell:											
1	17 413	5.622	27.37	45.908	44.165	46.508	−0.09	29.241	67.192	45.515	46.866
2	17 572	5.631	27.368	45.184	44.244	46.557	0.201	43.628	36.633	68.59	43.628
3	17 737	5.634	27.392	44.593	43.922	45.98	−0.087	63.203	35.929	82.594	63.203
4	17 901	5.637	27.435	45.911	44.458	47.013	0.145	38.371	−26.04	62.352	38.371
5	18 065	5.653	27.493	45.203	44.344	46.66	0.108	51.92	73.965	−2.372	51.92
6	18 225	5.647	27.555	44.629	43.997	46.054	−0.106	71.68	130.307	54.848	71.68
7	18 389	5.64	27.603	46.024	44.435	46.954	0.046	64.407	65.551	58.118	64.407
8	18 549	5.665	27.638	45.308	44.399	46.76	0.127	48.989	15.779	29.079	48.989
9	18 713	5.644	27.668	44.703	44.062	46.138	−0.094	40.989	8.011	13.466	40.989
10	18 878	5.64	27.683	46.04	44.528	47.078	0.099	4.303	−21.442	4.034	4.303
11	19 042	5.644	27.695	45.312	44.443	46.783	0.108	70.087	87.191	31.845	70.087
12	19 207	5.637	27.703	44.706	44.087	46.149	−0.103	41.028	55.826	28.199	41.028
13	19 371	5.637	27.706	46.015	44.6	47.151	0.139	29.351	31.31	4.118	29.351
14	19 536	5.65	27.716	45.3	44.464	46.776	0.089	76.269	96.532	41.062	76.269
15	19 695	5.656	27.717	44.713	44.104	46.158	−0.106	36.664	57.737	−0.065	36.664
16	19 859	5.637	27.726	46.117	44.534	47.054	0.04	29.722	54.444	2.661	29.722
17	20 019	5.64	27.731	45.387	44.488	46.847	0.117	84.894	87.412	62.14	84.894
18	20 183	5.631	27.739	44.77	44.143	46.218	−0.097	52.182	61.635	22.024	52.182
19	20 348	5.613	27.741	46.242	44.443	46.908	−0.072	36.168	31.269	23.033	36.168
20	20 507	5.634	27.733	45.474	44.513	46.92	0.136	92.497	101.152	70.495	92.497
21	20 672	5.613	27.729	44.845	44.188	46.299	−0.072	48.61	62.14	15.364	48.61
22	20 831	5.609	27.719	46.313	44.268	46.598	−0.165	32.99	64.041	6.986	32.99
23	20 990	5.644	27.703	45.575	44.535	46.983	0.17	83.599	106.511	24.246	83.599
24	21 154	5.631	27.678	44.925	44.239	46.387	−0.047	87.482	181.967	24.082	87.482
25	21 314	5.625	27.648	45.799	44.051	46.198	−0.224	59.341	70.183	42.443	59.341
26	21 478	5.637	27.604	45.654	44.539	47.019	0.17	56.747	32.967	25.296	56.747

Table B.1. continued.

Index	Elapsed time	Foreoptics pressure	Laser plate temp	Foreoptics temp	Ref cell temp	Science detector temp	HCell pressure	e line in situ CH_4 ppbv	f line in situ CH_4 ppbv	g line in situ CH_4 ppbv	Wefg in situ CH_4 ppbv
Sol 2627 Full Cell:											
1	12 178	4.735	17.398	45.102	43.476	47.196	4.493	96.858	39.346	77.644	72.873
2	12 338	4.738	17.198	44.181	43.069	46.437	4.264	57.152	76.598	83.676	75.275
3	12 502	4.732	17.034	45.488	43.371	47.132	4.348	27.895	71.229	69.67	59.616
4	12 662	4.738	16.917	44.481	43.174	46.731	4.366	66.894	77.132	94.356	83.185
5	12 826	4.726	16.82	45.769	43.22	46.94	4.292	94.114	33.329	75.191	69.456
6	12 985	4.748	16.75	44.712	43.275	46.974	4.431	54.829	41.091	69.206	58.583
7	13 144	4.779	16.69	44.264	42.795	46.156	4.183	59.191	30.906	81.093	63.071
8	13 308	4.853	16.649	45.043	43.331	47.142	4.462	83.383	61.699	83.888	78.215
9	13 473	4.785	16.599	44.087	42.91	46.4	4.252	42.474	28.241	52.369	43.863
10	13 637	4.8	16.572	45.354	43.343	47.248	4.438	51.993	80.44	59.548	62.882
11	13 802	4.81	16.562	44.307	43.042	46.644	4.323	72.725	39.622	55.639	55.906
12	13 966	4.791	16.561	45.648	43.065	46.828	4.218	13.005	52.872	74.456	53.697
13	14 131	4.831	16.569	44.576	43.137	46.881	4.413	93.65	96.656	79.338	87.246
14	14 295	4.807	16.585	45.249	42.898	46.524	4.183	50.671	81.238	82.99	74.472
15	14 459	4.838	16.617	44.78	43.228	47.06	4.462	91.973	79.674	63.843	74.833
16	14 618	4.825	16.661	44.435	42.807	46.309	4.221	66.095	46.637	106.365	81.365
17	14 783	4.831	16.714	45.037	43.307	47.223	4.481	45.338	63.178	59.31	56.784
18	14 942	4.844	16.793	44.126	42.935	46.49	4.273	70.041	11.668	86.093	63.474
19	15 106	4.819	16.89	45.453	43.208	47.099	4.314	94.35	95.051	76.402	85.551
20	15 271	4.834	16.991	44.423	43.07	46.765	4.369	32.097	64.492	50.872	49.583
21	15 435	4.819	17.09	45.689	43.122	46.926	4.252	66.341	82.194	52.149	63.208
22	15 594	4.862	17.147	44.667	43.215	46.986	4.431	66.279	84.568	22.271	48.847
23	15 753	4.85	17.175	44.201	42.764	46.179	4.196	71.358	73.162	50.798	61.529
24	15 917	4.853	17.185	45.043	43.285	47.169	4.472	103.032	45.575	42.899	58.601
25	16 082	4.862	17.183	44.111	42.93	46.444	4.273	132.152	99.681	46.11	81.013
26	16 246	4.844	17.171	45.427	43.218	47.071	4.323	87.723	72.157	58.756	69.348
Sol 2627 Empty cell:											
1	17 465	4.859	17.154	44.725	43.253	47.003	0.181	70.931	57.887	55.814	60.111
2	17 629	4.872	17.121	44.806	42.875	46.361	−0.088	64.623	90.572	37.636	64.623
3	17 794	4.875	17.088	44.914	43.306	47.126	0.215	48.54	42.492	49.173	48.54
4	17 958	4.859	17.058	44.109	42.875	46.324	−0.048	59.759	63.371	57.123	59.759
5	18 123	4.853	17.04	45.094	43.322	47.201	0.181	54.129	45.564	58.182	54.129
6	18 287	4.862	17.023	44.225	42.953	46.479	−0.005	66.604	120.043	41.226	66.604
7	18 452	4.862	17.01	45.144	43.383	47.299	0.184	57.068	25.677	69.746	57.068
8	18 616	4.841	17.018	44.167	43	46.55	−0.02	77.666	88.005	60.695	77.666
9	18 780	4.834	17.047	45.305	43.329	47.248	0.029	49.65	72.143	44.612	49.65
10	18 939	4.844	17.086	44.314	43.064	46.699	0.026	68.367	76.846	58.232	68.367
11	19 103	4.822	17.116	45.58	43.181	47.022	−0.091	47.011	46.357	33.111	47.011
12	19 263	4.834	17.126	44.513	43.142	46.874	0.079	53.04	55.258	58.344	53.04
13	19 427	4.813	17.13	45.704	43.231	47.105	−0.064	40.568	30.175	34.727	40.568
14	19 592	4.838	17.133	44.599	43.221	46.985	0.107	48.998	16.314	36.714	48.998
15	19 756	4.788	17.13	45.366	42.997	46.667	−0.185	67.578	117.265	28.196	67.578
16	19 920	4.81	17.121	44.739	43.255	47.085	0.116	36.355	68.864	15.503	36.355
17	20 085	4.788	17.11	45.451	43.06	46.774	−0.138	46.194	43.963	36.083	46.194
18	20 249	4.813	17.11	44.806	43.316	47.169	0.138	36.263	35.205	29.777	36.263
19	20 408	4.788	17.093	45.375	43.077	46.776	−0.132	50.505	75.263	30.269	50.505
20	20 572	4.788	17.068	44.859	43.358	47.232	0.144	38.594	33.369	47.818	38.594
21	20 737	4.794	17.04	44.537	42.893	46.414	−0.144	50.749	46.122	55.276	50.749
22	20 901	4.788	17.016	44.983	43.339	47.25	0.129	33.556	−4.1	38.468	33.556
23	21 066	4.772	16.993	44.605	42.927	46.504	−0.119	68.037	93.211	55.118	68.037
24	21 230	4.772	16.976	45.028	43.368	47.306	0.144	30.469	42.38	48.142	30.469
25	21 395	4.763	16.954	44.607	42.957	46.547	−0.107	52.528	61.555	41.044	52.528
26	21 559	4.772	16.924	45.052	43.392	47.344	0.138	50.172	44.636	66.473	50.172

Table B.1. continued.

Index	Elapsed time	Foreoptics pressure	Laser plate temp	Foreoptics temp	Ref cell temp	Science detector temp	HCell pressure	e line in situ CH_4 ppbv	f line in situ CH_4 ppbv	g line in situ CH_4 ppbv	Wefg in situ CH_4 ppbv
Sol 2644.51 Full Cell:											
1	11 884	5.544	29.247	44.532	43.948	46.126	4.078	77.448	101.927	29.469	59.578
2	12 049	5.551	29.191	45.911	44.457	47.054	4.28	10.701	6.453	73.173	40.875
3	12 213	5.594	29.207	45.204	44.395	46.749	4.289	98.485	58.601	50.978	64.76
4	12 378	5.6	29.247	44.623	44.067	46.096	4.084	65.848	53.66	66.723	63.239
5	12 542	5.597	29.303	46.07	44.493	46.942	4.221	16.658	0.817	67.51	38.124
6	12 707	5.634	29.361	45.345	44.503	46.787	4.329	−34.303	66.373	69.575	42.805
7	12 871	5.644	29.426	44.768	44.196	46.172	4.115	−10.191	9.967	37.326	18.607
8	13 036	5.65	29.494	46.2	44.52	46.847	4.187	9.947	22.363	45.431	30.793
9	13 200	5.712	29.569	45.469	44.6	46.833	4.363	43.254	64.893	66.027	60.051
10	13 364	5.702	29.643	44.892	44.308	46.249	4.168	135.099	70.33	40.848	71.781
11	13 529	5.702	29.703	45.971	44.196	46.175	4.05	48.27	67.264	41.783	49.775
12	13 693	5.737	29.749	45.696	44.682	46.938	4.407	37.705	77.679	36.069	46.881
13	13 853	5.743	29.788	45.113	44.46	46.433	4.233	−5.969	56.475	82.74	53.997
14	14 017	5.786	29.814	44.724	44.113	45.85	4.094	−20.598	38.705	65.283	37.168
15	14 182	5.746	29.805	45.643	44.634	46.744	4.342	73.303	26.868	90.229	70.157
16	14 346	5.78	29.837	45.049	44.392	46.308	4.224	29.874	54.333	75.679	58.891
17	14 510	5.777	29.831	45.033	44.068	45.792	4.084	47.414	68.895	51.885	55.02
18	14 675	5.792	29.82	45.579	44.561	46.685	4.342	44.201	3.269	76.995	50.365
19	14 840	5.802	29.798	44.997	44.358	46.228	4.205	20.43	46.174	78.499	55.901
20	15 004	5.805	29.769	45.378	44.091	45.839	4.066	−15.964	85.294	59.565	47.115
21	15 168	5.839	29.735	45.845	44.729	46.947	4.441	20.466	19.277	103.975	61.923
22	15 333	5.839	29.695	45.237	44.551	46.497	4.295	9.21	51.932	61.2	45.886
23	15 497	5.83	29.652	44.734	44.213	45.934	4.112	−4.156	65.153	69.696	50.097
24	15 662	5.91	29.662	46.172	44.672	46.837	4.289	7.927	78.638	53.732	48.507
25	15 826	5.854	29.549	45.502	44.665	46.731	4.376	67.421	73.403	97.462	83.937
26	15 991	5.842	29.491	44.957	44.377	46.188	4.177	86.451	95.419	40.366	65.651
Sol 2644.51 Empty cell:											
1	17 213	5.842	28.994	44.763	44.208	45.976	−0.069	63.059	14.248	65.221	51.937
2	17 377	5.839	28.87	45.896	44.436	46.536	−0.041	48.965	32.947	50.53	48.965
3	17 542	5.864	28.749	45.236	44.419	46.451	0.086	76.79	119.988	29.202	76.79
4	17 706	5.83	28.639	44.698	44.109	45.911	−0.097	41.517	58.928	6.811	41.517
5	17 870	5.826	28.534	45.796	44.404	46.58	−0.01	30.787	59.661	17.527	30.787
6	18 030	5.823	28.435	45.156	44.341	46.405	0.071	10.785	30.299	23.7	10.785
7	18 194	5.823	28.339	45.043	44.033	45.892	−0.14	43.618	22.087	50.856	43.618
8	18 353	5.82	28.246	45.606	44.501	46.765	0.12	34.536	13.546	42.746	34.536
9	18 517	5.792	28.155	44.987	44.274	46.301	−0.019	51.248	3.649	76.879	51.248
10	18 682	5.82	28.066	45.968	44.145	46.205	−0.202	51.926	41.79	75.574	51.926
11	18 846	5.795	27.978	45.388	44.424	46.667	0.083	82.337	103.26	73.217	82.337
12	19 157	5.792	27.84	45.882	44.44	46.771	−0.016	81.226	104.105	61.896	81.226
13	19 321	5.764	27.74	45.189	44.358	46.548	0.027	81.577	85.727	66.945	81.577
14	19 485	5.752	27.641	44.612	44.006	45.959	−0.171	47.076	36.749	41.093	47.076
15	19 650	5.749	27.536	45.929	44.539	47.01	0.096	52.172	27.077	64.829	52.172
16	19 814	5.743	27.438	45.232	44.395	46.651	0.043	17.995	−3.643	32.676	17.995
17	19 979	5.706	27.394	44.708	44.058	46.034	−0.156	46.798	39.594	56.437	46.798
18	20 143	5.727	27.23	45.601	44.438	46.847	0.068	73.483	41.591	89.788	73.483
19	20 302	5.718	27.133	44.962	44.211	46.371	0.049	76.089	66.278	79.26	76.089
20	20 466	5.712	27.024	45.477	43.931	46.022	−0.249	65.478	100.975	32.082	65.478
21	20 631	5.733	26.91	45.322	44.286	46.666	0.046	25.877	7.373	45.214	25.877
22	20 795	5.693	26.8	44.691	43.989	46.11	−0.146	61.812	74.875	80.244	61.812
23	20 960	5.684	26.692	45.657	44.353	46.853	0.027	41.858	43.049	58.413	41.858
24	21 124	5.668	26.578	44.966	44.154	46.426	−0.063	19.348	22.384	42.383	19.348
25	21 289	5.653	26.458	45.799	43.98	46.205	−0.171	66.847	64.49	53.091	66.847
26	21 453	5.668	26.347	45.272	44.245	46.689	0.024	63.441	80.944	37.77	63.441

Plots of individual data points from Table B.1

The *y*-axis units are in situ CH_4 average abundance Wefg in ppbv. The *x*-axis identifies each of the 26 sequential measurement points. Empty-cell measurements always immediately follow full-cell measurements.

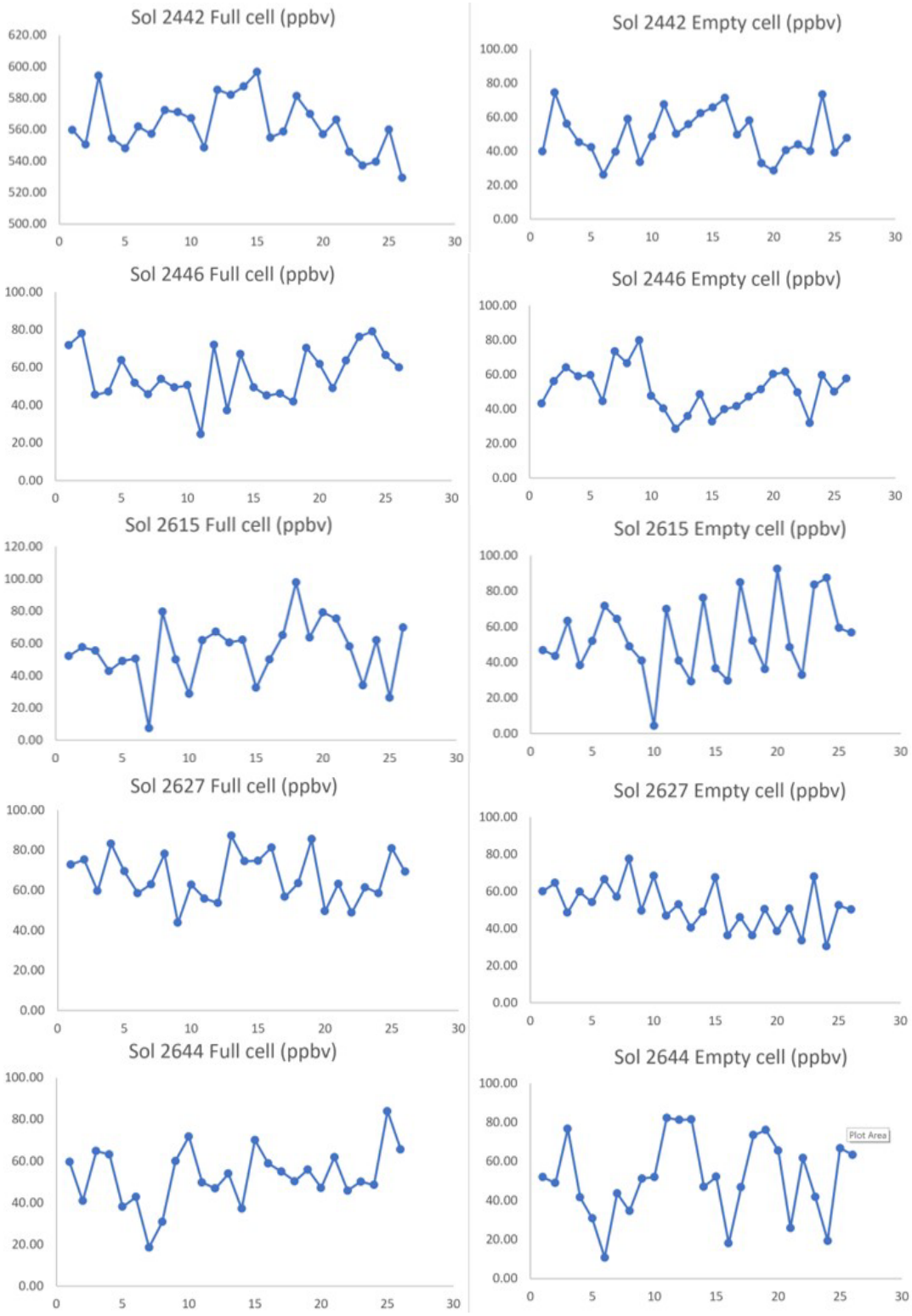

Fig. B.1. Plots of individual data points from Table B.1.